

High Resolution Calculations of Merging Neutron Stars I: Model Description and Hydrodynamic Evolution

Stephan Rosswog, Melvyn B. Davies

Department of Physics and Astronomy, University of Leicester, LE1 7RH, Leicester, UK

Accepted 2002 January 31. Received 2002 January 17; in original form 2001 September 4

ABSTRACT

We present the results of 3D high resolution calculations of the last inspiral stages and the final coalescence of neutron star binary systems. The equations of hydrodynamics are solved using the smoothed particle hydrodynamics method with up to 10^6 particles. Using Newtonian gravity, but adding the forces emerging from the emission of gravitational waves, we focus on the impact of microphysics on the dynamical evolution of the merger. Namely we use a new equation of state based on the relativistic mean field approach of Shen et al. (1998a,b). Neutrino emission of all flavours, the resulting cooling and the change in the electron fraction are accounted for with a detailed leakage scheme.

The new equation of state is substantially stiffer than the Lattimer-Swesty equation of state that has been used in previous investigations. This leads the system to become dynamically unstable at a separation as large as 3.3 stellar radii, where the secular orbital decay undergoes a transition towards a dynamical “plunge” of the binary components towards each other. As soon as the stars come into contact a Kelvin-Helmholtz-instability forms at the interface of both stars. The peak temperatures are found in the vortex rolls that form during this process. We generally find slightly lower temperatures than previously found using the Lattimer-Swesty equation of state.

The central object is surrounded by a very thick disk that shows cool equatorial flows: inflows in the inner parts of the disk and outflow further out. The cool inflows become shock heated in the innermost parts of the disk and lead to an outflow of hot material in the vertical direction. The temperatures in the disk have typical values of 3-4 MeV, lower than the temperatures found in previous investigations using the Lattimer-Swesty equation of state. These conditions allow for the existence of heavy nuclei even in the inner parts of the disk, we find typical mass fractions of ~ 0.1 , which is enough for scattering off heavy nuclei to be the dominant source of neutrino opacity.

The central object formed during the coalescence shows a rapid, differential rotation with periods of ~ 2 ms. Although a final conclusion on this point is not possible from our basically Newtonian approach, we argue that the central object will remain stable without collapsing to a black hole, at least on the simulation time scale of 20 ms, mainly stabilized by differential rotation. The massive, differentially rotating central object is expected to wind up initial magnetic fields to enormous field strengths of $\sim 10^{17}$ G (Duncan & Thompson 1992) and may therefore have important implications for this event as a central engine of Gamma Ray Bursts.

Key words: dense matter; hydrodynamics; neutrinos; gamma rays: bursts; stars: neutron; methods: numerical

1 INTRODUCTION

The final stage of the inspiral and the subsequent coalescence of a neutron star binary system is among the prime

candidates for ground based gravitational wave detection via the laser interferometers currently under construction such as LIGO (Abramovici et al., 1992), TAMA (Kuroda et al., 1997), VIRGO (Bradaschia et al., 1990) and GEO (Danz-

mann, 1997). The neutron star merger scenario could also provide the energy reservoirs to power cosmological gamma ray bursts (GRB; Paczyński (1986); Eichler et al. (1989)) and is in addition one of the two most discussed production sites of the heavy, rapid neutron capture elements (Lattimer & Schramm, 1974, 1976; Symbalisty & Schramm, 1982; Eichler et al., 1989; Rosswog et al., 1999; Freiburghaus et al., 1999). Whether this scenario can fulfil all these promises or not, neutron star binary systems are known to exist and to inevitably coalesce (Taylor, 1994). This fact alone - apart from all further promises - justifies a careful study of the coalescence process and its possible implications.

The coalescence is an intrinsically three-dimensional phenomenon and therefore analytical guidance is rare although very welcome and one has to resort to large scale computations. Additional complications arise from the fact that there is almost no field of astrophysics that does not enter at some stage during the coalescence process: the last stages and the merger are certainly dominated by strong-field general relativistic gravity, the neutron star material follows the laws of hydrodynamics, particle physics enters via possible condensates of “exotic” matter in the high-density interiors of the neutron stars and the copiously produced neutrinos in the hot and dense neutron star debris, questions concerning element formation require detailed information on nuclear structure and reactions (often far from stability) to be included and also magnetic fields might play a decisive role since they may, via transport of angular momentum, determine whether and/or when the central, coalesced object collapses into a black hole.

Due to this complexity current investigations follow one of two “orthogonal” lines: either ignoring microphysics, resorting to the simplest equations of state (EOS), polytropes, and thereby focusing on solving the complicated set of general relativistic fluid dynamics equations (or some approximation to it) or, along the other line, using Newtonian self-gravity of the fluid and investigating the influences of detailed microphysics and relating the merger event to astrophysical phenomena.

Many groups have performed 3D calculations of the merger scenario. The first work, using a polytropic EOS and Newtonian gravity, was performed by Oohara & Nakamura (1997, and references therein) using Eulerian finite difference codes. Rasio & Shapiro (1992, 1994, 1995), Zhuge et al. (1994, 1996) and Davies et al. (1994) have used the smoothed particle hydrodynamics method (SPH) to further explore various aspects of the scenario.

The strong-field gravity aspect of the event was explored again by Oohara & Nakamura (1997, and references therein) using Post-Newtonian hydrodynamics in Eulerian formulation. Recently, Post-Newtonian calculations have also been performed using SPH by Ayal et al. (2001), Faber & Rasio (2000) and Faber et al. (2001). Several groups have worked on general relativistic formulations where the metric has been treated in the conformal flatness approximation (Wilson & Mathews, 1995; Oohara & Nakamura, 1997; Baumgarte et al., 1997; Oechslin et al., 2001). Recently, much progress has been made towards a stable implementation of the fully relativistic equations of hydrodynamics (Shibata, 1999; Shibata & Uryu, 2000).

The line relying on (basically) Newtonian gravity and investigating the microphysics of the event has been explored by

Ruffert et al. (1996, 1997) and Ruffert & Janka (2001) using a grid code based on the piecewise parabolic method (PPM) and by Rosswog et al. (1999, 2000) using SPH.

In this paper we want to continue to explore the impact of the microphysics on the outcome of the coalescence. We use a new equation of state that overcomes previous restrictions in the temperature and density. Since the high density regime of the nuclear physics is only poorly known to date this work will unfortunately not provide the final answer, but further broaden our understanding of the large effects that can be expected from the nuclear physics input. The calculations to be described below were performed on parallel computers allowing for an unprecedented hydrodynamic resolution.

The paper is organized as follows. In Section 2 we describe the basic ingredients like the hydrodynamics or the equation of state of our model. Section 3 describes the initial conditions of our calculations, the overall hydrodynamic evolution, and then focuses on aspects concerning the central object and the debris, referred to as “disk”. The summary and a discussion of the results are provided in Section 4.

2 MODEL

2.1 Hydrodynamics

To follow the dynamical evolution of the neutron star fluid we use a Lagrangian particle scheme, the so-called smoothed particle hydrodynamics method (SPH; Benz (1990); Monaghan (1992)). Since it is independent of any prescribed geometry (e.g. grid) it is perfectly suited to handle the intrinsically three-dimensional merger process. In addition, the Lagrangian nature of the scheme makes it easy to carefully track the evolution of interesting portions of the fluid (e.g. possible ejecta). Voids are treated in a natural way (i.e. no particles) and do not present any difficulty for the method, the interesting parts of the simulation do not have to be embedded in an artificial background medium like in other methods (e.g. PPM). The use of a background medium leads to further difficulties like emerging (artificial) shock waves at the stellar surfaces that have to be treated by additional remedies (Ruffert & Janka, 2001). If the corresponding parameters are not chosen carefully, the artificial medium may also lead to a damping of (physical) oscillations (Font et al., 2000).

Since SPH is well-known we will only describe the basic ingredients of our code. The basic set of equations may be found in Benz (1990). Rather than the “standard” form of *artificial viscosity* (AV; Monaghan & Gingold (1983)) we use a hybrid method that profits from two improvements: the viscosity parameters are time dependent (Morris & Monaghan, 1997) and have non-negligible values only in the presence of shocks. Additionally, a switch is applied that suppresses spurious forces in pure shear flows (Balsara, 1995). This hybrid method (Rosswog et al., 2000) has been shown to resolve shocks with the same accuracy as the standard formulation of AV, but exhibits much better behaviour in shear flows. In test calculations of differentially rotating stars the viscous time scales $\tau_{visc,i} = v_i/\dot{v}_{i,visc}$ obtained with the new scheme were two orders of magnitude longer than those from the standard form of AV. For details and test calculations

we refer to Rosswog et al. (2000).

Since it is a widespread belief that SPH is always extremely viscous by nature, we want to measure the effective “alpha-viscosity”, α_{ss} , defined by Shakura & Sunyaev (1973)

$$\nu = \alpha_{ss} c_s H, \quad (1)$$

where ν is the kinematic viscosity, c_s the sound velocity and H the disk thickness. In 3D the SPH bulk viscosity parameter, α (see e.g. Monaghan (1992)), can be related to the kinematic viscosity via (Murray (1995))

$$\nu = \frac{\alpha}{10} c_s h, \quad (2)$$

where h is the smoothing length. Due to the modifications in our hybrid AV-scheme we use $\tilde{\alpha}_i = \alpha_i \cdot f_i$ in the above formula rather than the bulk viscosity parameter of particle i , α_i . Here f_i is the Balsara-factor implemented in our code,

$$f_i = \frac{|\nabla \cdot \vec{v}|_i}{|\nabla \cdot \vec{v}|_i + |\nabla \times \vec{v}|_i + \eta c_{s,i}/h_i} \quad (3)$$

and $\eta = 10^{-4}$. This factor suppresses AV in pure shear flows ($f_i \rightarrow 0$ for $|\nabla \times \vec{v}| \gg |\nabla \cdot \vec{v}|$) where it is unwanted, and $f_i \rightarrow 1$ in the case of pure shocks ($|\nabla \times \vec{v}| \ll |\nabla \cdot \vec{v}|$). Equating (1) and (2) one finds

$$\alpha_{ss,i} = \frac{\tilde{\alpha}_i h_i}{10 H}, \quad (4)$$

i.e. apart from the numerical value $\tilde{\alpha}_i$ it is the resolution of the disk that determines the effective alpha-viscosity α_{ss} . It should, however, be noted that this relation is only approximate since the effects of AV and the α -viscosity prescription are not necessarily exactly the same and due to the way the Balsara-factor is taken into account. To obtain numerical values we insert the average thickness of the central object and disk of run B (see below; Table 1) into equation (4). By averaging according to

$$\langle \alpha \rangle_{ss} = \frac{\sum_i m_i \alpha_{ss,i}}{\sum_i m_i}, \quad (5)$$

where m_i are the particle masses, we find

$$\langle \alpha \rangle_{ss} = \begin{cases} 6 \cdot 10^{-4} & \text{all particles} \\ 4 \cdot 10^{-3} & \text{debris} \\ 3 \cdot 10^{-5} & \text{central object} \end{cases}$$

For details of concerning “debris” and “central object” see below. These values are very low in comparison with the values that are derived from observations of cataclysmic variables, $\alpha \sim 0.1$, and it is certainly possible that the physical viscosity of a hot neutron star debris disk is much higher than the values of the above determined numerical viscosity.

The (Newtonian) forces of the *self-gravity* of the fluid are efficiently calculated using a binary tree (Benz et al., 1990). Since the computationally most expensive part of the code is the evaluation of gravitational forces we implemented an *integrator* for the set of differential equations that only needs one force evaluation per time step. We decided to implement an Adams-Bashforth method which is third order accurate in time. This allows for a very accurate conservation of energy and angular momentum even with relative large step sizes. In a calculation with $\sim 100\,000$ particles these quantities are conserved to a few parts in 10^4 over $\sim 10\,000$ time steps. For reasons of comparison: other schemes (Ruffert &

Janka, 2001) lose up to 10 % of the total angular momentum by numerical artifacts despite excellent energy conservation. The amount of noise present in SPH depends, of course, on the particle distribution. For the worst case, a stochastic particle distribution, it scales like $1/\sqrt{N_N}$, where N_N is the number of neighbours a particle interacts with. Therefore while increasing the total particle number, N , one should also increase the number of neighbours in order to reduce the noise level. On the other hand one is not interested in too large an increase of the neighbour number and therefore the smoothing length, h , since it would compromise the spatial resolution and the numerical error; remember that the SPH-equations are accurate to order $O(h^2)$. Therefore, N_N should increase slower than N . In the calculations presented here typical neighbour numbers are 100-120.

Our whole code is parallelized for use on shared memory machines using OpenMP. For particle numbers above $\sim 400\,000$ we find an almost linear speedup for up to 120 processors.

2.2 Gravitational Wave Back-reaction

The forces emerging from the emission of gravitational waves that drive the binary towards coalescence are treated in the point mass limit of the quadrupole approximation and are applied until the stars come into contact. Since each particle in a star is subject to the same back-reaction force the conservation of the fluid circulation is guaranteed. For a further discussion of this approach we refer to Rosswog et al. (1999).

2.3 Equation of State

The equation of state (EOS) is one of the most crucial ingredients of a neutron star simulation and the microscopic behaviour of matter decisively determines the overall, macroscopic evolution of the system (compare, for example, the calculations using a polytrope versus those with the nuclear EOS of Lattimer & Swesty (1991) [LS-EOS] in Rosswog et al. (1999)). Since the stiffness of the EOS varies over a wide range as a function of density, temperature and composition (see below) and the release of nuclear binding energy when nucleons form nuclei has important dynamical consequences, a simple polytropic EOS is only a poor approximation of the involved microphysics. All neutron star merger calculations that used a nuclear equation of state (Ruffert et al., 1996, 1997; Ruffert & Janka, 2001; Rosswog et al., 1999, 2000) relied on the Lattimer-Swesty-EOS. This EOS, however, has been designed for the use in supernova-calculations and therefore suffers from some deficiencies in our context: the electron fraction, Y_e , is restricted to values above ~ 0.04 , temperatures to values above $\sim 10^9$ K and densities above 10^7 gcm $^{-3}$. The electron fraction in a neutron star in β -equilibrium, however, dips down to values of ~ 0.01 near the neutron star surface (see below) and temperatures in old neutron stars are expected to be negligible with respect to typical nuclear energies; viscous heating during the inspiral is expected to increase the temperatures to only $\sim 10^8$ K (Lai, 1994). Therefore, once outside the EOS-range, these investigations either used extrapolation (Ruffert et al., 1996) or kept the EOS-quantities at the boundary values (Rosswog et al., 1999).

In this work we use an EOS based on the tables of Shen et al. (1998a,b) that overcomes all above mentioned restrictions, in the electron fraction as well as in temperature and density. Shen et al. follow a relativistic mean field (RMF) approach which reproduces the basic features of more complicated relativistic Dirac-Brückner-Hartree-Fock calculations. The starting point is a relativistically covariant Lagrangian that contains, apart from the nucleon fields, the scalar σ , and the ω and ρ vector mesons. For the σ and ω meson fields non-linear terms are included, which are essential to reproduce quantitative properties of nuclei (e.g. the compression modulus) correctly. The parameter set (TM1, Sugahara & Toki (1994)) is chosen in a way that experimental data of finite nuclei in the ground as well as in excited states are satisfactorily reproduced. With this parameter set the compression modulus, K_0 , has a value of 281 MeV, whereas in the Lattimer-Swesty EOS in Ruffert et al. (1996), Rosswog et al. (1999) and all comparisons in this paper $K_0 = 180$ MeV has been used. Since many-body interactions at high densities are only poorly constrained to date, no effort is made to include more “exotic” physics such as hyperons, various mesons or quark matter in the high density regime. At densities above $\sim 1/3 \rho_{nuc}$ protons and neutrons form a homogeneous “nucleon fluid”, below this density matter may become inhomogeneous, i.e. the presence of nuclei may become energetically favorable. This phase is modelled using the Thomas-Fermi approximation. Matter is assumed to consist of a mixture of nucleons, alpha-particles and spherical nuclei arranged on a lattice. The heavy nucleus (representative of a distribution of heavy nuclei) is assumed to be centered in a charge neutral cell consisting of vapor of the neutrons, protons and alpha particles. Above $\rho \approx 10^{10}$ g cm $^{-3}$ the nucleons are treated by the RMF theory, below this density they are assumed to form a Maxwell-Boltzmann gas. The alpha-particles are treated as a non-interacting Boltzmann gas, their occupied volume is accounted for in the calculation of the free energies. The density distribution in the Wigner-Seitz cell is parametrized and the free parameters are determined by minimizing the free energy density with respect to the densities of all ingredients.

Shen et al. only provide the baryonic part of the EOS. Their tables range from 0 to 100 MeV in temperature, 0 to ~ 0.56 in Y_e and 5.1 to 15.4 in $\log(\rho)$ (ρ in cgs-units). We therefore add the contributions from photons and electron-positron pairs to the baryonic components. For the electron-positron pairs we use the code of Timmes & Arnett (1999). Apart from disregarding interactions, which is perfectly justified at the high densities of interest, the electron-positron-pairs are treated in full generality without any approximation. In the low density regime, $\rho < 10^5$ g cm $^{-3}$, we extend the EOS with a gas consisting of neutrons, alpha-particles, electron-positron pairs and photons. The smooth transition is demonstrated in Figure 1. The EOS described above is tabulated with 32 entries in temperature, 72 in electron fraction and 151 in density. We store the following quantities: total pressure, internal energy, difference in the nucleonic chemical potentials $\hat{\mu}$, sound velocity, entropy, mass fractions of protons (x_p), alpha particles (x_α) and the heavy nucleus (x_h), the proton to nucleon ratio, Z/A , and the nucleon number A of the heavy nucleus. The neutron mass fraction is obtained as $x_n = 1 - (x_p + x_\alpha + x_h)$.

In Fig. 2 we show a comparison between the pressures pro-

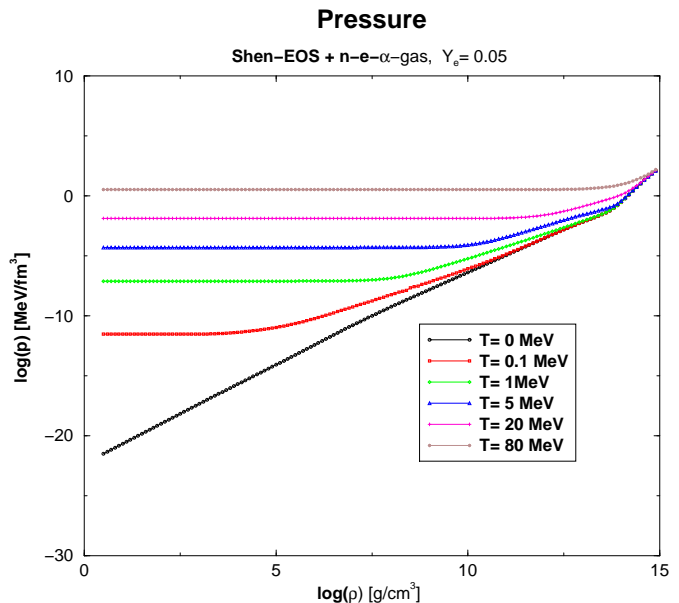


Figure 1. Pressure as a function of temperature for our EOS (baryonic part from Shen et al. + photons + electron-positron pairs, extension with a gas consisting of neutrons, alpha particles, electron-positron pairs and photons). The transition between the original EOS and the extension lies at $\rho \approx 10^5$ g/cm 3 .

pressure LS-EOS and Shen et al. EOS

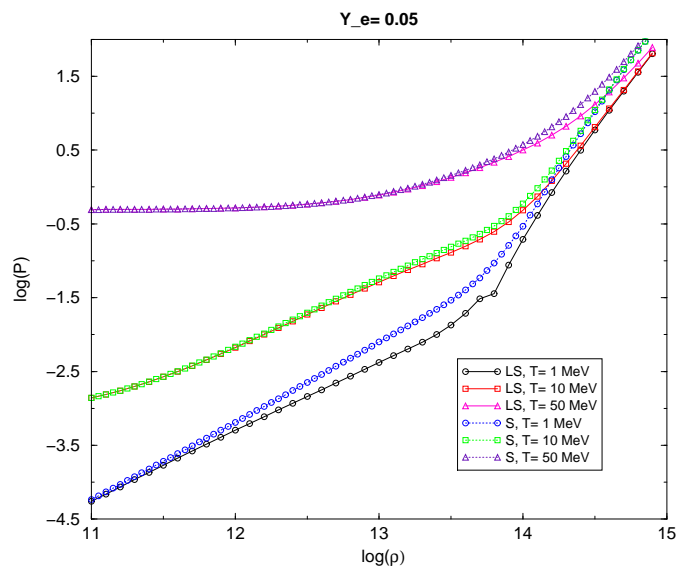


Figure 2. Comparison of the pressures provided by the Lattimer-Swesty and the Shen et al. EOS as a function of density (cgs-units).

vided by both the LS-EOS and the EOS of Shen et al. Below 10^{11} g cm $^{-3}$ the results are practically identical, at higher densities the new EOS is substantially stiffer than the LS-EOS. For rather low temperatures ($T = 1$ MeV) we find large differences in the density range from 10^{12} to 10^{14} g cm $^{-3}$, which is the density regime that is crucial for the torus that forms around the central object, see below. For even higher densities the pressure curves for different temperatures converge indicating the diminishing relevance of

thermal pressure contributions. Again, the Shen et al. EOS yields considerably higher pressure values.

The Shen-EOS also yields larger values for $\hat{\mu}$. Since the neutrino-less β -equilibrium value of the electron chemical potential is given by $\bar{\mu}_e = \hat{\mu} - Q$, Q being the neutron proton mass difference, and Y_e is a monotonic function of $\bar{\mu}_e$ the Shen-EOS yields higher values for Y_e than the LS-EOS.

2.4 Neutrino Physics

The emission of neutrinos provides a very efficient cooling mechanism for hot neutron star matter and the related electron and positron captures change the electron fraction Y_e which in turn determines the matter composition. We include the most important neutrino reactions where we ensure, via effective rates, that only the amount of neutrinos is produced that is actually able to leave the dense surrounding material. Our scheme takes careful account of the energy dependence of the neutrino opacities by integrating over the neutrino distributions.

For the emission processes we include electron captures (EC)



and positron captures (PC)



which produce electron flavour neutrinos and the pair producing reactions, pair annihilation



and plasmon decay



Here $\bar{\nu}_i/\nu_i$ refer to anti-/neutrinos of all types.

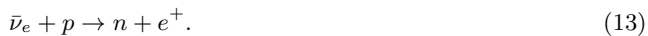
For the opacities we include the dominant processes, neutrino nucleon scattering



coherent neutrino nucleus scattering



and neutrino absorption by nucleons



Note that this is the first time that the effects of scattering off heavy nuclei have been accounted for in a neutron star merger calculation. These are important whenever nuclei are present since the corresponding cross sections scale proportional to A^2 and $A \approx 80$ (see below). For details of this transport scheme we refer to Rosswog et al. (2002), where the neutrino emission results are discussed in detail.

3 RESULTS

3.1 Initial Conditions

3.1.1 Neutron Star Masses

We focus in this investigation on equal mass systems with $1.4 M_\odot$ per star since all well-determined neutron star masses

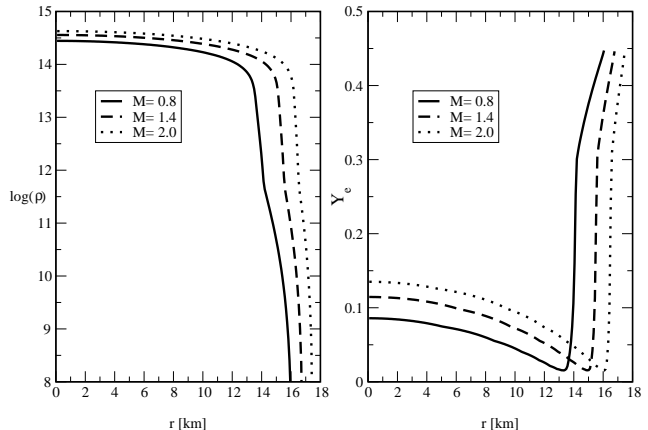


Figure 3. Profiles of matter density and electron fraction of the initial neutron star models (masses in solar units).

from radio binary pulsars are distributed according to a narrow distribution around $1.4 M_\odot$ (Thorsett & Chakrabarti, 1999). For neutron stars in X-ray binary systems substantially higher masses have been claimed: e.g. $1.8 \pm 0.2 M_\odot$ for CygX-2 (Orosz & Kuulkers, 1999), $\sim 1.9 M_\odot$ for VelaX-1 (J.H. van Kerkwijk & Zuiderwijk, 1995) and $1.8 \pm 0.4 M_\odot$ for 4U 1700-37 (Heap & Corcoran, 1992). In order to get an upper limit we additionally explore the case of twice $2.0 M_\odot$ (see Table 1).

It should be noted that the system dynamics is extremely sensitive to even small deviations from a mass ratio of unity. This sensitivity to the mass difference has been explored previously, both using a polytropic (Rasio & Shapiro, 1994) and a realistic EOS (Rosswog et al., 2000; Ruffert & Janka, 2001) and will not be the subject of this investigation.

3.1.2 Neutron Star Models

We solve the one dimensional hydrostatic structure equations together with the neutrino-less β -equilibrium condition to find the properties of the initial neutron stars. Examples of such initial profiles are shown in Fig. 3. Note the enormous density decrease at the neutron star surface which is caused by the stiffness of the Shen-EOS. This effect is more pronounced for the higher mass neutron stars, low mass stars possess a thicker crust, as is visible from both density and Y_e -profile. To illustrate this stiffness we show in Fig. 4 the quantity $\tilde{\Gamma} = \text{dln}(p)/\text{dln}(\rho)$ obtained by finite differencing along a neutron star profile of $1.4 M_\odot$. $\tilde{\Gamma}$ rises from values close to 3 in the center to ~ 3.2 to drop sharply at the phase transition towards inhomogeneous matter and remain around 1.3 in the neutron star crust.

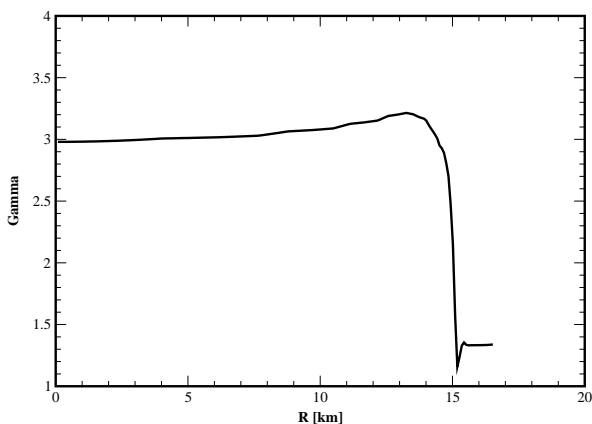
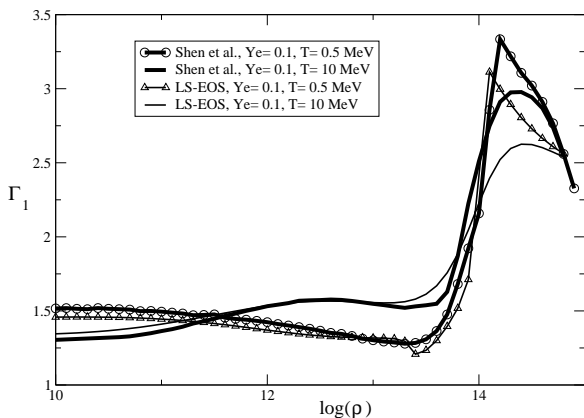
To compare once again with the LS-EOS, we plot in Fig. 5 the adiabatic exponent Γ_1 , given by (Cox & Giuli, 1968)

$$\Gamma_1 = \frac{\rho}{p} \left(\frac{\partial p}{\partial \rho} \right) + T \left(\frac{\partial p}{\partial T} \right)^2 \left(\rho p \frac{\partial u}{\partial T} \right)^{-1}, \quad (14)$$

where T is the temperature and u the specific internal energy, for both the Shen-EOS and the LS-EOS in the relevant low- Y_e regime, $Y_e = 0.1$. In the case of the Shen-EOS the

Table 1. Summary of the different runs. a_0 : initial separation; ν : neutrino physics; T_{sim} : simulated duration; M_1/M_2 : masses in solar units; # part.: total particle number

run	spin	M_1	M_2	# part.	a_0 [km]	ν	T_{sim} [ms]
A	corot.	1.4	1.4	207,918	48	no	10.7
B	corot.	1.4	1.4	1,005,582	48	no	10.8
C	irrot.	1.4	1.4	383,470	48	yes	18.3
D	corot.	1.4	1.4	207,918	48	yes	20.2
E	irrot.	2.0	2.0	750,000	48	yes	12.2

**Figure 4.** $\tilde{\Gamma} = \ln(p)/\ln(\rho)$ along a neutron star profile of 1.4 M_{\odot} .**Figure 5.** Shown is the variation of Γ_1 with density (cgs-units) and temperature for a fixed electron fraction, $Y_e = 0.1$, for both our equation of state (Shen et al. plus extension) and the Lattimer-Swesty-EOS.

derivatives in (14) have to be obtained by finite differencing, in the LS-EOS case they are available from analytical expressions. For the cold case, $T = 0.5$ MeV, Γ_1 rises from values of ~ 1.5 at $\log(\rho) = 10$ to values of ~ 3.3 for the Shen-EOS and ~ 3.1 for the LS-EOS. Note the sharp peak at $\log(\rho) \approx 14$ which is present in both EOSs. In the high temperature case, $T = 10$ MeV, the maximum values are slightly lower and the peaks are smeared out. This variation of Γ_1 with the physical conditions demonstrates again the difficulty of approximating a nuclear EOS by a polytrope of fixed adiabatic exponent.

The electron fraction, Y_e , decreases from central values of around 0.1 (higher values are encountered for more massive stars) to values as low as ~ 0.01 and increases steeply again towards the surface (Fig. 3). Note that only a tiny amount of material, $\sim 1\%$ of the star's mass, is located in this region of increasing Y_e .

3.1.3 Initial Spins and Separation

Since the time during which the neutron stars can tidally interact is extremely short it would need an implausibly high neutron star viscosity to lead to a tidal locking of the binary components during the inspiral phase (Bildsten & Cutler, 1992; Kochanek, 1992). The spins at the moment of merger will be negligible with respect to the orbital angular momentum and therefore the most realistic spin configuration is close to the irrotational case. Thus, the most interesting configuration to be explored is the case without initial neutron star spins. We also investigate corotating systems for reasons of completeness and since it is straightforward to construct equilibrium configurations by damping out velocities in the corotating frame. For details of this procedure we refer to Rosswog et al. (1999). The case of neutron stars spinning in the direction opposite to the orbit has been explored in previous work (Ruffert et al., 1996; Rosswog et al., 1999) and shall not be further discussed here.

The neutron stars with the corresponding spins are then set to Keplerian orbits and are provided with radial velocities corresponding to

$$\dot{a}_0 = -\frac{64}{5} \frac{G^3 M^2 \mu}{c^5 a_0^3}, \quad (15)$$

where a_0 is the initial separation, M the total and μ the reduced mass (e.g. Shapiro & Teukolsky (1983)). For further details we refer to Rosswog et al. (1999). Starting with spherical stars is obviously not an equilibrium configuration and will therefore result in oscillations of the stars. We have tried to reduce these oscillations by stretching the stars ac-

Figure 6. Mass distribution in the orbital plane. The labels indicate contours of $\log(\rho)$, ρ is in g cm^{-3} . The left column corresponds to a corotating system (more than 10^6 particles, run B) the right one to a system without initial neutron star spins (more than 700 000 particles, run E). The orbital motion is counter-clockwise.

Figure 7. Left column: velocity field and density contours in the orbital plane in the corotating frame for an initially corotating configuration ($> 1\,000\,000$ particles, run B). Shown is the central object only (down to $\log(\rho) = 13.5$, ρ in g cm^{-3}). Right column: corresponding temperatures.

cording to the ellipsoidal approximation of Lai et al. (1994a) for polytropes of $\Gamma = 3$ (compare Fig. 4) and correcting for the finite size effects in the corresponding orbital frequency. However, this did not improve the calculations, we therefore started the calculation with spherical stars and Keplerian orbital frequency. At the chosen initial separation (see below) the tidal deformations of the stars are very small, the height of the tidal bulge being $h \approx (R_*/a_0)^3 R_* \approx 0.03 R_*$, where R_* is the neutron star radius.

The initial separation has to be determined as a tradeoff between computational resources and physically reasonable initial conditions. Binary systems can become dynamically unstable (i.e. they coalesce on a *dynamical* time scale) due to entirely Newtonian tidal effects (Chandrasekhar, 1975; Tasoul, 1975). This means that orbital decay changes abruptly from the secular orbital decay driven by the emission of gravitational waves to a rapid plunging of both components towards each other on just the orbital time scale. The reason for this instability is the steeping of the effective interaction potential between both components due to tidal effects. Tidal effects increase with the incompressibility of the stellar fluid (since the stars are less centrally condensed) and therefore the onset of this dynamical instability is a very sensitive function of the stiffness of the EOS, setting in at larger separations for a stiffer EOS. This instability has been studied extensively in Newtonian gravity using an ellipsoidal approximation to the neutron star shape (Lai et al. (1994a) and references therein). Relativistic effects shift the innermost stable circular orbit, R_{ISCO} , to larger binary separations (Baumgarte et al., 1998a,b).

We determined the binary separation where the system becomes dynamically unstable experimentally. To this end a binary configuration was relaxed in the mutual tidal field, set to a corotating orbit and evolved for several orbits without radial velocity and back-reaction force. This experiment again underlined the enormous stiffness of the EOS which translated in a (for a Newtonian calculation) very large separation for the ISCO. We found a corotating binary to be stable for an initial separation of $R_{\text{dyn}} = 49.5$ km, corresponding to $R_{\text{ISCO}}/R_* \approx 3.3$. We therefore chose the initial separation for the simulation start as $a_0 = 48$ km, which we regard to be an acceptable compromise between computational effort and physical appropriateness.

The simulations performed are summarized in Table 1. We use particle numbers up to 10^6 which translates into smoothing lengths of ≈ 0.38 km in the initial neutron stars.

3.2 Overall Hydrodynamic Evolution

Since we start our simulation just inside the last stable orbit the neutron stars approach each other very quickly and merge within roughly one orbital revolution. Being con-

stantly kept back by a slowly receding centrifugal barrier the merger itself proceeds very subsonically (keep in mind that typical sound velocities are $\sim 0.4 c$).

The corotating systems (runs A, B, D) merge within approximately one orbital period. Prior to merger only a tiny lag angle develops between the axes of the neutron stars (first panel, left column Fig. 6). Note that such a lag angle develops even in absence of viscosity since the system is not able to adapt fast enough to the rapidly changing tidal potential (Lai et al., 1994b). Immediately after contact mass shedding via the outer Lagrangian points sets in which results in thick, puffed up spiral arms (Fig. 6), that subsequently wrap around the central object to form a disk. The spiral arms show an appreciable lateral expansion and soon engulf the central object and the innermost high-density parts of the disk (last panel, left column in Fig.6).

The irrotational configurations merge slightly quicker, the system with twice $1.4 M_\odot$ (run C) after around three-quarters of an orbit and the system with $2.0 M_\odot$ (run E; Fig.6) after half an orbit, due to the lower total angular momentum. This faster inspiral leads to noticeably larger lag angles before contact. The systems start immediately to shed hot material with rather low density from the interaction region. This is closely followed by mass shedding via the outer Lagrangian points. The matter that is shed by the latter mechanism whips through the previously ejected material forming a spiral shock which heats up the material. The spiral pattern is much less pronounced than in the corotating case and becomes washed out within a few milliseconds by lateral expansion and a rapidly expanding disk is left behind. The material within this disk follows eccentric trajectories and once the outward motion is reversed and matter starts falling back towards the hot compact remnant in the centre, the inner parts of this torus-like structure become compressed and heat up. Note the enormous expansion of the debris material, in all cases the typical diameter of the mass distribution increases from ~ 100 km to ~ 1000 km in just a few milliseconds.

One may speculate that the stronger general relativistic gravity would lead to a more compact post-merger configuration with a more massive central object and a less massive torus around it. For polytropic calculations this tendency is indeed visible (Shibata & Uryu, 2001).

In Table 2 we show the (baryonic) masses contained in the central object and the debris material. Both regimes are discriminated on grounds of a $\log(\rho)$ -r-plot. In several cases the transition between central object and debris is rather smooth so that it is difficult to determine the exact mass cut. The resulting uncertainties are of the order $0.02 M_\odot$.

Figure 8. Left column: velocity field and density contours in the orbital plane in the corotating frame for a system without spins ($\sim 400\,000$ particles, run C). Shown is the central object only (down to $\log(\rho) = 13.5$, ρ in g cm^{-3}). Right column: corresponding temperatures.

Table 2. Final rest mass distribution, M_{co} refers to the mass of the central object and M_{deb} the mass of the debris material. a denotes the stability parameter Jc/GM_{co}^2 , where J is the angular momentum contained in the central object.

run	M_{co}	M_{deb}	a
A	2.33	0.47	0.48
B	2.35	0.45	0.49
C	2.55	0.25	0.64
D	2.33	0.47	0.48
F	3.71	0.55	0.55

3.3 Central Object

The central objects of all performed calculations do not become axisymmetric on the simulation time scale (Figs. 6,7,8) and will therefore continue to emit gravitational radiation. This result is in qualitative agreement with those from uniformly rotating stiff polytropes ($\Gamma > \Gamma_{\text{crit}} \approx 2.3$; Tassoul (2001)). Note that contrary to previous investigations (Davies et al., 1994; Rasio & Shapiro, 1994) we never end up with rigidly rotating central objects. This is an effect from the lower viscosity due to our new artificial viscosity scheme and the high resolution of the present calculations; the effective alpha-viscosities in the central object are $\sim 10^{-5}$, see Section 2.1.

It has been pointed out previously by various authors (Ruffert et al., 1996; Rosswog et al., 1999; Rasio & Shapiro, 1999; Faber et al., 2001) that a vortex sheet forms between the stars as soon as they come into contact. This is most pronounced for the irrotational case, since, in the frame corotating with the binary, the stars seem to be spinning in opposite directions and therefore a discontinuous velocity field is encountered when the interface between both stars is crossed. Such a vortex sheet is known to be Kelvin-Helmholtz unstable on all wave lengths, with the shortest modes growing fastest. As has been pointed out previously, the shortest growing mode is determined by the smallest, numerically resolvable length scale. For a further discussion of this point we refer to the previously mentioned literature.

The velocity field for the initially corotating system is shown in column one in Fig. 7. Along the vortex sheet two vortices form which remain well-separated and which are not dissipated until the end of the simulation. In Fig. 8 the velocity fields in a frame corotating with the binary system are shown (orbital plane, central object only) for the spinless system. The vortex sheet is clearly visible in the first panels of Figs. 7 and 8. The Kelvin-Helmholtz instability creates a set of vortices along the interaction interface. These merge during the further evolution leaving behind a rapidly, differentially rotating merger remnant. As will be discussed below, this has important consequences for the stability of the central object.

To further illustrate the differential rotation of the merged

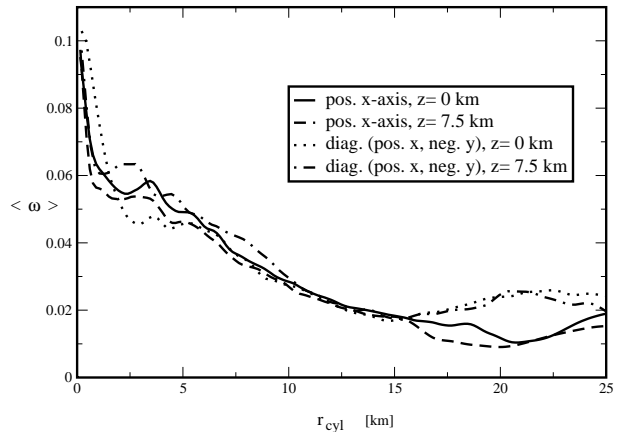


Figure 9. Differential rotation of the merged remnant I: snapshot of the angular frequencies (displayed in code units of $1.984 \cdot 10^5$ 1/s), of the most realistic initial configuration, run C, at $t = 7.686$ ms (compare Fig. 8) along the positive x-axis (for two different heights) and along a diagonal (positive x, negative y; again two heights). The increase of ω towards the origin corresponds to the central vortex (see Fig. 8).

remnant we show in Fig. 9 the SPH-smoothed values of the angular frequency

$$\langle \omega \rangle(\vec{r}) = \sum_j \frac{v_{\text{tan},j}}{r_{\text{cyl},j}} \frac{m_j}{\rho_j} W(|\vec{r} - \vec{r}_j|, h_j), \quad (16)$$

where \vec{r} is the point of interest (see below), $v_{\text{tan},j}$ is the cylindrical tangential velocity of particle j , $r_{\text{cyl},j} = \sqrt{x_j^2 + y_j^2}$, m_j and ρ_j are mass and density and W is the used spline-based SPH-kernel (e.g. Monaghan (1992)). We only show the case of no initial spins (run C), since it is the most relevant one (the corotating case is apart from the persistent vortices closer to rigid rotation). The chosen time, $t = 7.686$ ms, corresponds to the last panels, column one and two in Fig. 8. We show $\langle \omega \rangle$ along the positive x-axis, both at the height of $z = 0$ and $z = 7.5$ km, and along a diagonal given by positive x-values and negative y-values, since this line is an approximate symmetry-axis at this stage (again for heights of $z = 0$ and $z = 7.5$ km). $\langle \omega \rangle$ is strongly peaked at the centre, where the central vortex is located and decays with increasing distance from the origin depending on the direction and height above the orbital plane. The corresponding periods, $\langle T \rangle = 2\pi/\langle \omega \rangle$ are shown in Fig. 10. The central 10 km of all chosen lines have periods below 1 ms.

The highest temperatures of the merged configuration are found in the above mentioned vortices, see right columns Figs. 7 and 8. The maximum temperatures inside the central objects are shown in Fig. 11. Due to the high degeneracy of the neutron star matter oscillations due to imperfect initial conditions and numerical noise lead to temperatures of a few MeV, however only in the dense, central regions

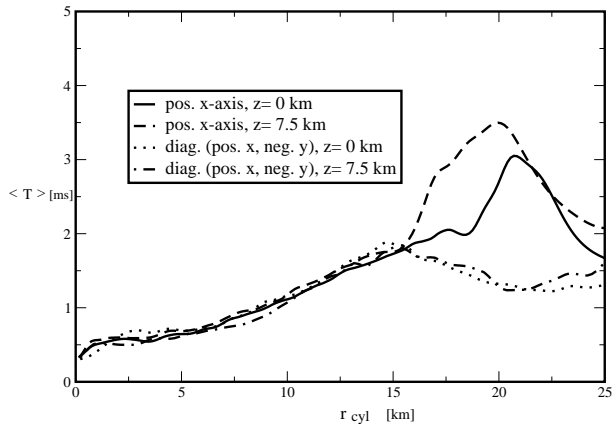


Figure 10. Differential rotation of the merged remnant II: periods (in ms) corresponding to Fig. 9.

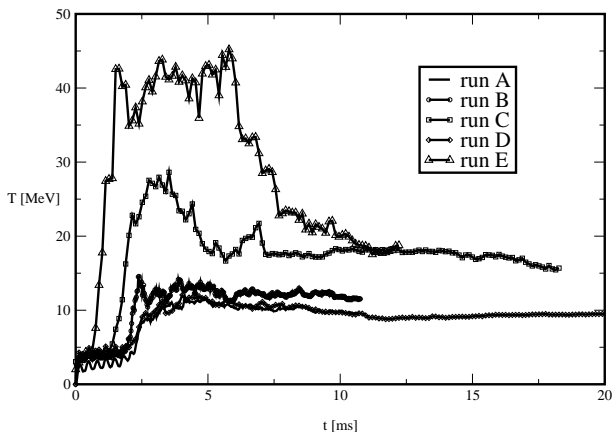


Figure 11. Maximum temperatures (in MeV) in the merged configurations as a function of time (ms).

where these finite temperatures have no physical effect (no thermal pressure contribution at these densities; matter is opaque to neutrinos). In the case of corotation the temperature hardly rises above the level during inspiral. Due to the larger shear motion irrotational initial conditions yield substantially higher maximum temperatures: up to ~ 30 MeV in the case of $1.4 M_{\odot}$ and ~ 45 MeV for our extreme case of $2.0 M_{\odot}$ stars. These temperatures are lower than those reported by Ruffert et al. (1996). This may be an effect of the different masses used in both investigations (1.4 versus $1.6 M_{\odot}$), the different EOS (compare also Ruffert & Janka (2001), Fig. 15) and different numerical viscosities in both codes.

We find the masses of the central objects to be roughly $0.1 M_{\odot}$ lower, see Table 2, than those of previous calculations using the softer Lattimer-Swesty EOS (Rosswog et al., 1999).

The question whether/when the central object collapses to

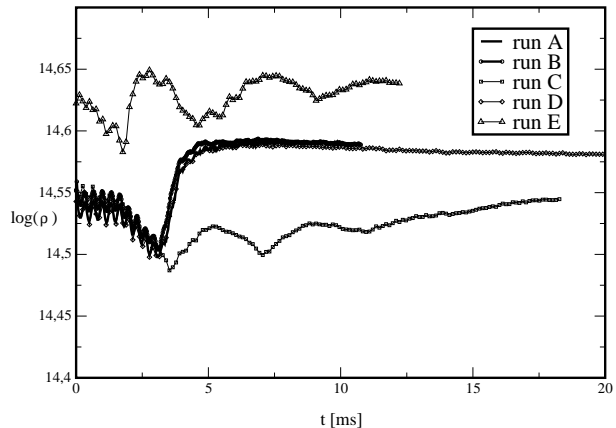


Figure 12. Maximum densities of the different runs as a function of time (measured in ms). Shown is the $\log(\rho)$ with ρ in g cm^{-3} .

a black hole is relevant for various reasons, e.g. to decide on possible mechanisms to produce Gamma Ray Bursts (GRBs). Most state of the art nuclear equations of state can support cold, non-rotating neutron stars in β -equilibrium of $\sim 2.2 M_{\odot}$ gravitational mass (Akmal et al., 1998). This corresponds approximately to the baryonic masses we find here for the central objects. Recent relativistic mean field equations of state are able to stabilize even heavier neutron stars (between 2.45 and $3.26 M_{\odot}$, (Chung et al., 2001)). Therefore even cold, non-rotating configurations of the masses found here may be supported by most of these EOSs. Additional stabilizing effects come from the finite, thermal contributions to the pressure. If the matter further contains non-leptonic, negative charges such as Σ^{-} hyperons, d or s quarks, then trapped neutrinos lead to an additional increase of the maximum mass (Prakash et al., 1995). The initial magnetic field of neutron stars, $B_0 \sim 10^{12}$ G, is expected to be amplified in the differentially rotating remnant to enormous field strengths, $\sim 10^{17}$ G (Duncan & Thompson, 1992), which, again, leads to a substantial increase of the maximum mass (Cardall et al., 2001). Stark & Piran (1985) have analyzed the stability of a rotating polytrope against the collapse towards a black hole. For the investigated case of *rigid* rotation they found that rotation can stabilize the fluid against collapse if the stability parameter $a = Jc/GM^2$ is larger than ≈ 1 . The stability parameters a of the central objects in our calculations are ~ 0.5 and are shown for completeness in Table 2. We expect the most important stabilizing effect to come from the *differential* rotation of the merger remnant. The enormous increase in the maximum mass by differential rotation has been demonstrated for the case of white dwarfs by Ostriker & Bodenheimer (1968) who constructed configurations up to $4.1 M_{\odot}$. Recent general relativistic treatments of differentially rotating neutron stars (Baumgarte et al., 2000) find that even modest degrees of differential rotation allow for significantly higher maximum masses than non or uniformly rotating configurations.

It may be somewhat bold to speculate from an essentially Newtonian calculation about the stability of the remnant,

but from the above line of argument we are tempted to conclude that the central object remains stable at least on the simulation time scale, ~ 20 ms. Due to our ignorance of the high-density equation of state, it cannot be ruled out that the end product of the coalescence is a stable supermassive neutron star of $\sim 2.8 M_{\odot}$. It seems, however, more likely that the central object is only temporarily stabilized and once the stabilizing effects weaken (e.g. neutrinos have diffused out after ~ 10 s, magnetic braking has damped out differential rotation) collapse to a black hole will occur. The time scale until collapse is difficult to determine, since it depends sensitively on poorly known physics and on the specific system parameters. We expect the most important effect to come from the differential rotation Ostriker & Bodenheimer (1968); Baumgarte et al. (2000) and therefore the collapse time scale to be set by the time it takes the remnant to reach uniform rotation. Assuming the dominant effect to come from magnetic dipole radiation (the viscous time scale is estimated to be $\sim 10^9$ s (Shapiro, 2000)), the time till collapse is estimated as

$$\begin{aligned} \tau_c &\sim \frac{18c^3 M}{5B^2 R^4 \omega^2} \\ &\sim 10^2 s \left(\frac{M}{2.5M_{\odot}} \right) \left(\frac{10^{16} \text{G}}{B} \right)^2 \left(\frac{15 \text{km}}{R} \right)^4 \left(\frac{3000 \text{s}^{-1}}{\omega} \right)^2 \end{aligned} \quad (17)$$

where M, B and R are mass, magnetic field and radius of the central object.

3.4 Disk

Immediately after contact the two merged stars try to get rid of excess angular momentum by shedding mass. We refer to this debris material as 'disk'. In all cases, a few milliseconds after contact a thick disk, with typical heights roughly comparable to the disk radius, has formed around the central object (see Figs. 6, 14 and 15). The masses contained in the debris material are, depending on the initial spin, between 0.25 for run C and 0.55 M_{\odot} for our extreme case, run E.

Initially, as the material is being shed by the central object, the debris material is cooled via the very fast expansion. Part of this material is later shock-heated as subsequently ejected material runs into it. This is most pronounced in the case of initial corotation. Here the spiral arms expand laterally due to the released nuclear energy from recombination of nucleons into nuclei and due to the change in the adiabatic exponent and hit supersonically. This heating mechanism is illustrated for a run A in Fig. 13.

Fig. 14 shows disk properties in the orbital plane for the most realistic, initially non-spinning, configuration. The shedded mass follows eccentric trajectories, resulting in a fast initial expansion and cooling phase during the outward motion (see panel one, left column in Fig. 14) and a subsequent compression when the motion is reversed and the inner parts start to fall back towards the central object (see panel one, column two in Fig. 14), against material that is still being shed and moving outwards.

To illustrate the interplay between the fluid motion, the temperature and the vertical disk structure, we show in Fig. 15 the velocity fields together with density contours (left column) for run B (twice 1.4 M_{\odot} , corotation), run C (twice 1.4

M_{\odot} , no initial spins) and our extreme case, run E (twice 2.0 M_{\odot} , no initial spins). The corresponding temperatures are shown in the right column. The disk shows violent convective motion, that can be subdivided into roughly four flow regimes: (i) the innermost, shock-heated 'torus', that results from the collision of the hot matter shed from the central object and the cool ($T < 1$ MeV) equatorial inflow; (ii) the cool, equatorial inflow phase; (iii) a rarefaction regime that separates the inflow from the outflow and (vi) the cooling outflow from the disk. As the inflow hits the torus it drives a hot, vertical outflow which leads to the thick (H \sim R), puffed up disk. Only the innermost, high density material of the debris has temperatures in excess of ≈ 4 MeV, the shocked torus is at around 3 MeV, the hot, high-altitude outflow with densities below 10^9 g cm $^{-3}$ has temperatures between 1 and 2 MeV, the outer parts of the flow close to the equatorial plane are substantially cooler (see also Fig. 14, column two, panel two). In Fig. 16 we show a blow-up of the velocity fields (run B and E) in the regime where the cool inflow hits the inner parts of the disk and produces the "butterfly-shaped" temperature distribution. The temperatures found are slightly lower than those reported by Ruffert & Janka (2001) (up to 10 MeV). We suspect the stiffness of the Shen-EOS in the range between 10^{12} and 10^{14} g cm $^{-3}$, see Fig. 2, to be partly responsible for this fact.

Despite the high temperatures we still find a substantial mass fraction of heavy nuclei in the inner parts of the disk, which dominate the neutrino emission. We find roughly 10 % of the disk mass in the form of heavy nuclei (third panels in columns one and two of Fig.14). The Shen-EOS yields in the inner torus regime an average nucleus with $A \sim 80$ and $Z \sim 0.3$. We find for the ratio of the mean free path due to scattering off heavy nuclei, λ_A , and off free nucleons, λ_n , $\lambda_A/\lambda_n = n_n \sigma_n / (n_A \sigma_A) \approx 4(1 - X_h)/(X_h A) \approx 0.5$. Therefore *the scattering mean free path in these regions is dominated by heavy nuclei*. These have not been accounted for in previous investigations, which assumed the torus to be fully photo-disintegrated (Ruffert et al., 1996).

In Fig. 17 we plot the logarithm of the angular velocities as a function of the cylindrical radius for runs B, C and E and compare it to the corresponding Keplerian angular velocities. For runs B and C the innermost parts of the disk, up to ~ 100 km, are roughly Keplerian. Further out, up to ~ 300 km the disk rotates sub-Keplerian and the outermost, outflowing parts rotate faster than the corresponding Keplerian value. The disk of run E is roughly Keplerian out to ~ 200 km, drops below the Kepler value between ~ 200 and ~ 450 km and is above it at larger radii.

4 SUMMARY AND DISCUSSION

We have performed high-resolution 3D calculations of the last moments of the inspiral and the final coalescence of a neutron star binary system. Our main motivation was to explore the impact of the, sometimes poorly known, microphysics on the merger scenario.

The equations of hydrodynamics were solved using the smoothed particle hydrodynamics method with particle numbers of more than 10^6 to resolve the details of the thermodynamic and nuclear evolution. The initial neutron stars are resolved with smoothing lengths of ≈ 0.38 km. We

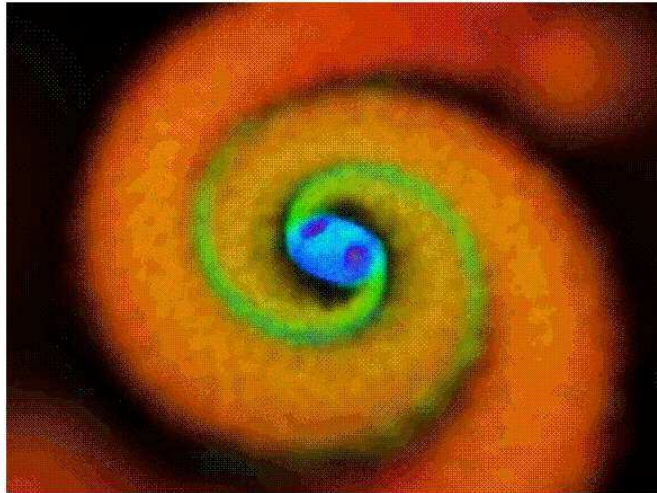


Figure 13. Disk heating mechanism: temperatures of the central region shortly after the merger ($t = 5.225$ ms, corotation, ~ 200000 particles, run A). The disk is shock-heated when the spiral arms hit supersonically due to their lateral expansion (green). The two hot spots (dark blue) in the central object stem from the vortices which formed during the Kelvin-Helmholtz instability during the merger (see text).

Figure 14. Physical properties of the disk (equatorial plane) that forms around the central object (no initial spins, run C). Shown are snapshots $t = 7.434$ ms (left column) and $t = 11.214$ ms (right column).

have measured the effective alpha-viscosity of our code and find for the well-resolved calculations values of $\langle \alpha \rangle_{SS} \approx 6 \cdot 10^{-4}$. The self-gravity of the fluid was treated in a Newtonian fashion, but forces from the emission of gravitational waves were added.

In these calculations the temperature-dependent, microscopic behaviour of the matter is modelled using a new nuclear equation of state whose baryonic part is described in the relativistic mean field approach (Shen et al., 1998a,b). We have added the contributions of electron-positron pairs (treated without any approximation) and photons to the baryonic component. In the low density regime the equation of state has been extended with a gas consisting of neutrons, alpha particles, electron-positron pairs and photons. This new EOS covers the whole parameter space in density, temperature and electron fraction that is relevant to the neutron star merger scenario and therefore overcomes the restrictions inherent to previous calculations using a different equation of state (Ruffert et al., 1996; Rosswog et al., 1999).

We have also included the change in the electron fraction, Y_e , and internal energy due to the emission of neutrinos by means of a detailed multi-flavour neutrino treatment that accounts carefully for the energy dependence of the neutrino reactions. In contrast to previous calculations scattering off heavy nuclei was included as a source of opacity.

The new equation of state is substantially stiffer than the previously used Lattimer-Swesty EOS, with adiabatic exponents reaching values well above 3 within a $1.4 M_\odot$ star. This has several important implications. First, since the stars are less centrally condensed the binary system becomes dynamically unstable at a larger separation. Since the inspiral behaviour changes qualitatively at this point from a quasi-stationary, quasi-periodic motion to a dynamic “plunge” to-

wards each other the gravitational wave signal will change correspondingly at this point. For a corotating system of $1.4 M_\odot$ we find the instability to set in at a separation of ~ 49 km and an orbital frequency of ≈ 280 Hz corresponding to ≈ 560 Hz in the gravitational wave signal, well within the range accessible to GEO600 and LIGO (Schutz & Ricci, 2001).

Once the neutron stars come into contact a Kelvin-Helmholtz unstable vortex sheet forms between both stars leading to the formation of vortex rolls. In the case of an initially corotating system two such vortices form which remain present and well-separated until the end of the calculation. In the more important irrotational case, several vortices form which merge within an orbital time scale leaving behind a differentially rotating central object. It is within these vortex roles that the highest temperatures of the merged configuration are found, reaching peak values of 30 MeV for the case of an irrotational system, while in the corotating case only a moderate temperature increase is observed. In a test calculation using two stars of $2.0 M_\odot$ temperatures of up to 45 MeV are reached. We find generally comparable but slightly lower temperatures than previous investigations that used the Lattimer-Swesty EOS.

The disks have a vertical height comparable to their radial extension. We find the vertical disk structure to be determined by an equatorial inflow of cool material that becomes shock heated in the innermost, dense disk regime. This goes along with an outflow of hot material in the vertical direction. In the dense inner torus around the central object we find temperatures of 3-4 MeV as compared to 5-10 MeV in the Lattimer-Sesty case. Despite the high temperatures we find a substantial amount (a mass fraction of $\sim 10\%$) of heavy nuclei present even in the inner parts of the torus. This is enough to dominate the neutrino scattering opacities

Figure 15. Vertical disk structure: density contours and velocity fields of runs B, C and E at around 10.7 ms are shown in the left column; the right column shows the temperature distribution (densities above 10^{12} g cm^{-3} are cut out to enhance the contrasts).

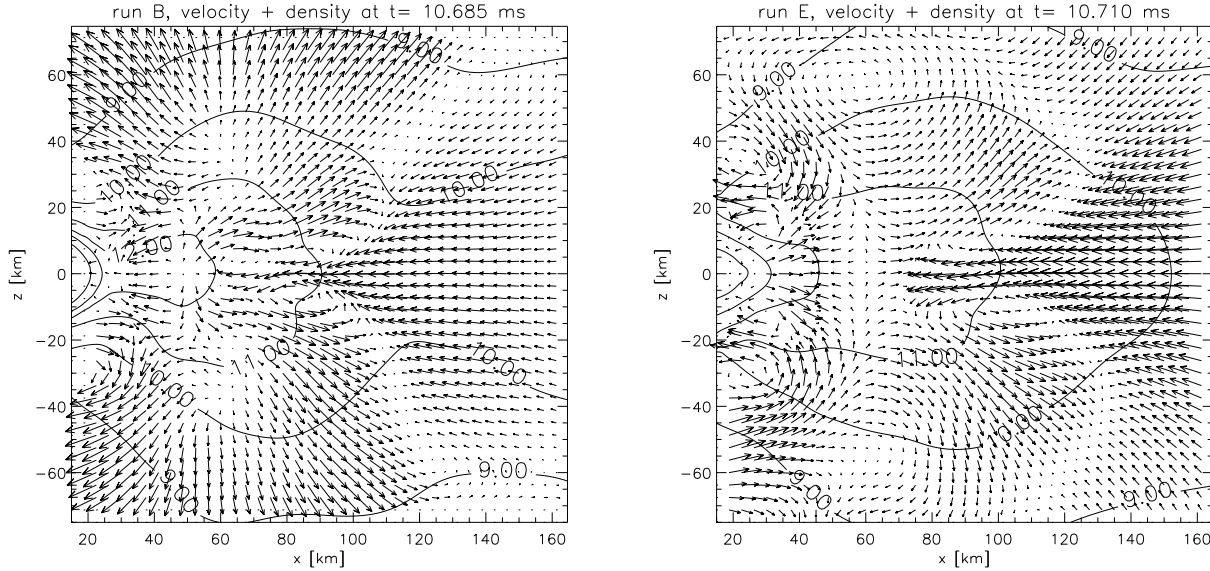


Figure 16. Blow-up of the velocity fields of the inner disk regions of run B and E (compare to Fig. 15).

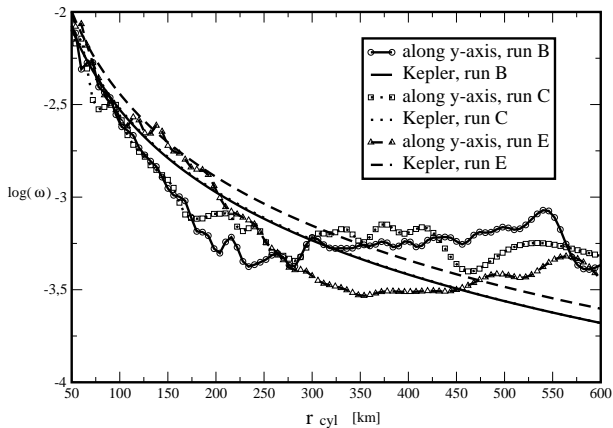


Figure 17. Plotted is the logarithm of the angular velocities (in code units of $1.984 \cdot 10^5$ 1/s) along the y-axis as a function of the cylindrical radius for runs B (circles; $t = 10.685$ ms), C (squares; $t = 10.710$ ms) and E (triangles; $t = 10.710$ ms). This is compared to the corresponding Keplerian angular velocities.

which therefore play a crucial role for the neutrino transport. This has important consequences for the enormously temperature sensitive neutrino reactions and will be discussed in a future paper.

The masses of the central objects are roughly $0.1 M_{\odot}$ lower than in previous calculations where we used the Lattimer-Swesty-EOS, leading to masses of the central object that are comparable to the maximum masses that most recent

nuclear equations of state can support for cold, non-rotating configurations. Since several stabilizing effects like thermal pressure contributions, rotation and, most likely, magnetic fields are active during the coalescence, we suspect the central object will remain stable on at least the simulation time scale of 20 ms. Probably the most important stabilisation comes from differential rotation. For the most probable case, where the neutron star spins are negligible with respect to the orbital motion, the maximum density of the central object barely reaches the initial central density of a single neutron star although its mass is roughly one solar mass higher. We estimate that the central objects could be stabilized against collapse for as long as $\sim 10^2$ s. It has to be stressed, however, that none of the equations of state used so far contains particles more exotic than nucleons. The appearance of more exotic matter in the deep cores of neutron stars is still subject to large uncertainties due to poorly constrained many-body interactions at highest densities. Therefore final conclusions on this point cannot be drawn.

If the central object indeed remains stable magnetic fields may wind up to reach $\sim 10^{17}$ G for a typical rotation period of 2 ms (Duncan & Thompson, 1992) and may therefore provide the conditions for magnetically-powered gamma ray bursts.

Acknowledgements

It is a pleasure to thank the Leicester supercomputer team Stuart Poulton, Chris Rudge and Richard West for their excellent support.

S.R. wishes to thank M.R. Bate for useful discussions. Most of the computations reported here were performed using the UK Astrophysical Fluids Facility (UKAFF). Part of this work has been performed using the University of Leicester Mathematical Modelling Centre's supercomputer which was purchased through the EPSRC strategic equipment initiative. This work was supported by a PPARC Rolling Grant for Theoretical Astrophysics. MBD gratefully acknowledges the support of the Royal Society by a URF.

References

Abramovici A., Althouse W. E., Drever R. W. P., Gursel Y., Kawamura S., Raab F. J., Shoemaker D., Sievers L., Spero R. E., Thorne K. S., 1992, *Science*, 256, 325
 Akmal A., Pandharipande V., Ravenhall D., 1998, *Phys. Rev. C*, 58, 1804
 Ayal S., Piran T., Oechslin R., Davies M. B., Rosswog S., 2001, *ApJ*, 550, 846
 Balsara D., 1995, *J. Comput. Phys.*, 121, 357
 Baumgarte T., Cook G., Scheel M., Shapiro S., Teukolsky S., 1997, *Phys. Rev. Lett.*, 79, 1182
 Baumgarte T., Cook G., Scheel M., Shapiro S., Teukolsky S., 1998a, *Phys. Rev. D*, 57, 6181
 Baumgarte T., Cook G., Scheel M., Shapiro S., Teukolsky S., 1998b, *Phys. Rev. D*, 57, 7299
 Baumgarte T., Shapiro S., Shibata M., 2000, *ApJ*, 528, L29
 Benz W., 1990, in Buchler J., ed., *Numerical Modeling of Stellar Pulsations*. Kluwer Academic Publishers, Dordrecht, p. 269
 Benz W., Bowers R., Cameron A., Press W., 1990, *ApJ*, 348, 647
 Bildsten L., Cutler C., 1992, *ApJ*, 400, 175
 Bradaschia C. et al., 1990, *Nucl.Instrum. Methods Phys. Res. A*, 289, 518
 Cardall C., Prakash M., Lattimer J., 2001, *ApJ*, 554, 332
 Chandrasekhar S., 1975, *ApJ*, 202, 809
 Chung K., Wang C., Satiago A., Zhang J., 2001, *astro-ph/0102993*, 0, 0
 Cox, J.P. & Giuli, R.T. (1968), *Principles of Stellar Structure*, New York, Gordon & Breach
 Danzmann K., 1997, in *of Sciences T. N. Y. A.*, ed., *Proceedings of the 17th Texas Symposium on relativistic astrophysics and cosmology* New York
 Davies M. B., Benz W., Piran T., Thielemann F.-K., 1994, *ApJ*, 431, 742
 Duncan R., Thompson C., 1992, *ApJ*, 392, L9
 Eichler D., Livio M., Piran T., Schramm D. N., 1989, *Nature*, 340, 126
 Faber J., Rasio F., 2000, *Phys.Rev. D*62, p. 064012
 Faber J., Rasio F., Manor J., 2001, *Phys.Rev. D*63, p. 044012
 Font J., Dimmelmeier H., Gupta A., Stergioulas N., 2000, *astro-ph/0012477*
 Freiburghaus C., Rosswog S., Thielemann F.-K., 1999, *ApJ*, 525, L121
 Heap S., Corcoran M., 1992, *ApJ*, 387, 340
 J.H. van Kerkwijk J. v. P., Zuiderwijk E., 1995, *A&A*, 303, 497
 Kochanek C., 1992, *ApJ*, 398, 234
 Kuroda K. et al., 1997, in *Gravitational Wave Detection, Proceedings of the TAMA International Workshop on Gravitational Wave Detection* held at National Women's Education Centre, Saitama, Japan, on 12-14 November, 1996. Edited by K. Tsubono, M.-K. Fujimoto, and K. Kuroda. *Frontiers Science Series No. 20*. Universal Academy Press, Inc., 1997., p.309 Japanese gravitational wave observatory (jgwo). pp 309+
 Lai D., 1994, *MNRAS*, 270, 611
 Lai D., Rasio F., Shapiro S., 1994a, *ApJ*, 420, 811
 Lai D., Rasio F., Shapiro S., 1994b, *ApJ*, 423, 344
 Lattimer J. M., Schramm D. N., 1974, *ApJ*, (Letters), 192, L145
 Lattimer J. M., Schramm D. N., 1976, *ApJ*, 210, 549
 Lattimer J. M., Swesty F. D., 1991, *Nucl. Phys.*, A535, 331
 Monaghan J., 1992, *Ann. Rev. Astron. Astrophys.*, 30, 543
 Monaghan J., Gingold R., 1983, *J. Comp. Phys.*, 52, 374
 Morris J., Monaghan J., 1997, *J. Comp. Phys.*, 136, 41
 Murray, J.R., PhD thesis, Monash University (1995)
 Oechslin R., Rosswog S., Thielemann F.-K., 2002, accepted for publication in *Phys. Rev. D*, gr-qc/0111005
 Oohara K., Nakamura T., 1997, in *Relativistic Gravitation and Gravitational Radiation*. Cambridge University Press, Cambridge
 Orosz J., Kuulkers E., 1999, *MNRAS*, 305, 132
 Ostriker J., Bodenheimer P., 1968, *ApJ*, 151, 1089
 Paczyński B., 1986, *ApJ*, 308, L43
 Prakash M., Cooke J., Lattimer J., 1995, *Phys. Rev.*, D52, 661
 Rasio F., Shapiro S., 1992, *ApJ*, 401, 226
 Rasio F., Shapiro S., 1994, *ApJ*, 432, 242
 Rasio F., Shapiro S., 1995, *ApJ*, 438, 887
 Rasio F., Shapiro S., 1999, *Class. Quant. Grav.*, 16, R1
 Rosswog S., Davies M. B., Thielemann F.-K., Piran T., 2000, *A & A*, 360, 171
 Rosswog S. et al. 2002, in preparation
 Rosswog S., Liebendörfer M., Thielemann F.-K., Davies M. B., Benz W., Piran T., 1999, *A & A*, 341, 499
 Ruffert M., Janka H., 2001, *A & A*, 380, 544
 Ruffert M., Janka H., Schäfer G., 1996, *A & A*, 311, 532
 Ruffert M., Janka H., Takahashi K., Schäfer G., 1997, *A & A*, 319, 122
 Schutz B., Ricci F., 2001, *Gravitational Waves*, 1. edn. IoP, London
 Shakura, N.I. & Sunyaev, R.A., 1973, *A & A*, 24, 337
 Shapiro S.L., 2000, *ApJ*, 544, 397
 Shapiro S., Teukolsky S. A., 1983, *Black Holes, White Dwarfs and Neutron Stars*. Wiley & Sons, New York
 Shen H., Toki H., Oyamatsu K., Sumiyoshi K., 1998a, *Nuclear Physics*, A 637, 435
 Shen H., Toki H., Oyamatsu K., Sumiyoshi K., 1998b, *Prog. Theor. Phys.*, 100, 1013
 Shibata M., 1999, *Phys. Rev. D*, 60, 104052
 Shibata M., Uryu K., 2000, *Phys. Rev. D*, 61, 064001
 Shibata M., Uryu K., 2001, *astro-ph/0104409*
 Stark, R.F., Piran T., 1985, *Phys. Rev. Lett.*, 55, 891
 Sugahara Y., Toki H., 1994, *Nucl. Phys*, A579, 557
 Symbalisky E. M. D., Schramm D. N., 1982, *Astrophys. Lett.*, 22, 143
 Tassoul M., 1975, *ApJ*, 202, 803

- Tassoul M., 2001, *Stellar Rotation*. Cambridge University Press, Cambridge
- Taylor J., 1994, *Rev. Mod. Phys.*, 66, 711
- Thorsett S., Chakrabarti D., 1999, *ApJ*, 512, 288
- Timmes F., Arnett D., 1999, *ApJS*, 125, 277
- Wilson J. R., Mathews G., 1995, *Phys. Rev. Lett.*, 75, 4161
- Zhuge X., Centrella J., McMillan S., 1994, *Phys. Rev.*, D50, 6247
- Zhuge X., Centrella J., McMillan S., 1996, *Phys. Rev.*, D54, 7261

This figure "p8.gif" is available in "gif" format from:

<http://arxiv.org/ps/astro-ph/0110180v3>

This figure "p9.gif" is available in "gif" format from:

<http://arxiv.org/ps/astro-ph/0110180v3>

This figure "p10.gif" is available in "gif" format from:

<http://arxiv.org/ps/astro-ph/0110180v3>

This figure "p14.gif" is available in "gif" format from:

<http://arxiv.org/ps/astro-ph/0110180v3>

This figure "p15.gif" is available in "gif" format from:

<http://arxiv.org/ps/astro-ph/0110180v3>